SLAC-PUB-9536
October 2002

Accepted for publication in the Astrophysical Journal

Variability Time Scales of TeV Blazars Observed in the ASCA Continuous Long-Look X–ray Monitoring

Chiharu Tanihata[1,2], C. Megan Urry[3], Tadayuki Takahashi[1,2], Jun Kataoka[4],
Stefan J. Wagner[5], Greg M. Madejski[6], Makoto Tashiro[7], and Manabu Kouda[1,2]

ABSTRACT

Three uninterrupted, long (lasting respectively 7, 10, and 10 days) ASCA observations of the well-studied TeV-bright blazars Mrk 421, Mrk 501 and PKS 2155–304 all show continuous strong X–ray flaring. Despite the relatively faint intensity states in 2 of the 3 sources, there was no identifiable quiescent period in any of the observations. Structure function analysis shows that all blazars have a characteristic time scale of $\sim$ a day, comparable to the recurrence time and to the time scale of the stronger flares. On the other hand, examination of these flares in more detail reveals that each of the strong flares is not a smooth increase and decrease, but exhibits substructures of shorter flares having time scales of $\sim$10 ks. We verify via simulations that in order to explain the observed structure function, these shorter flares ("shots") are unlikely to be fully random, but in some way are correlated with each other. The energy dependent cross-correlation analysis shows that inter-band lags are not universal in TeV blazars. This is important since in the past, only positive detections of lags were reported. In this work, we determine that the sign of a lag may differ from flare to flare; significant lags of both signs were detected from several flares, while no significant lag was detected from others. However, we also argue that the nature of the underlying component can affect these values. The facts that all flares are nearly symmetric and that fast variability shorter than the characteristic time scale is strongly suppressed, support the scenario where the light crossing time dominates the variability time scales of the day-scale flares.

Subject headings: BL Lacertae objects: individual (Mrk 501, PKS 2155–304, Mrk 421) — galaxies: active — radiation mechanisms: non-thermal — X–rays: galaxies

---

[1] Institute of Space and Astronautical Science, 3-1-1 Yoshinodai, Sagamihara, 229-8510, Japan

[2] Department of Physics, University of Tokyo, 7-3-1 Hongo, Bunkyo-ku, Tokyo, 113-0033, Japan

[3] Space Telescope Science Institute, Baltimore, MD, 21218, USA

[4] Department of Physics, Tokyo Institute of Technology, Tokyo, 152-8551, Japan

[5] Landessternwarte Heidelberg, Konigstuhl, D-69117, Heidelberg, Germany

[6] Stanford Linear Accelerator Center, Stanford, CA, 943099-4349, USA

[7] Department of Physics, Saitama University, Urawa, Saitama, 338-8570, Japan

*Work supported in part by Department of Energy Contract DE-AC03-76SF00515.

Stanford Linear Accelerator Center, Stanford University, Stanford, CA 94309, USA

1. INTRODUCTION

Jets are among the most exciting (but also among the least understood) cosmic phenomena, being unusually efficient particle accelerators that can generate relativistic electron distributions, which in turn produce synchrotron and inverse Compton radiation. The jet power is generated near the central black hole, probably via the conversion of gravitational energy from accreting matter by an as-yet unknown mechanism. Blazars are Active Galactic Nuclei (AGN) possessing jets aligned close to the line of sight, and thus the observed emission is dominated by the Doppler-enhanced jet component (e.g. Blandford & Konigl 1979; Urry & Padovani 1995). This makes blazars ideal targets for studying jet physics.

Rapid variability or flaring, which is one of the major characteristic of blazars, provides important clues towards understanding the conditions in the jet. Variability of the synchrotron spectral component is most rapid above the νF_ν peak of the emission (Ulrich, Maraschi, & Urry 1997), which is measured in the infrared to X–ray energy range. X–rays provide an ideal means for studying variability because there is little contamination from emission sources other than the jet (e.g., galaxy or nuclear emission), and because integration times are limited only by statistics.

The blazars with peak synchrotron output in the X–ray range also emit strongly at γ–ray energies. The brightest of those have been detected in the TeV range with ground-based air-shower arrays. These so-called "TeV blazars" include Mrk 421 (Punch et al. 1992) and Mrk 501 (Quinn et al. 1996) as the brightest sources, and several other objects including PKS 2155–304 (Chadwick et al. 1999) at somewhat fainter TeV fluxes. In the TeV blazars, the X–ray emission probes the electrons accelerated to the highest energies; those electrons have the shortest synchrotron cooling times. The TeV blazars listed above have been well studied previously at the X–ray energies via numerous multi-wavelength monitoring campaigns (e.g., Mrk 421: Macomb et al. 1995, Maraschi et al. 1999, Takahashi et al. 2000; Mrk 501: Catanese et al. 1997, Kataoka et al. 1999, Sambruna et al. 2000; PKS 2155–304: Urry et al. 1997) However, it was only the recent *ASCA* "long look" at Mrk 421 (Takahashi et al. 2000), a 7-day uninterrupted continuous observation in April 1998, that showed rapid daily flares not previously resolved with sparser sampling. Indeed, the wealth of information from this *ASCA* observation strongly underlined the need to obtain similar high quality data for other blazars.

To optimize *ASCA* science in its eighth year, especially as the new generation of X–ray telescopes was becoming available, the AO-8 program was explicitly devoted to long observations of interesting targets. We therefore proposed two 10-day campaigns for the next two X–ray brightest TeV blazars, Mrk 501 and PKS 2155–304. Our goal was to probe the physical conditions in the blazar jets. When events in the jet (such as shocks or changes in the magnetic field) cause changes in the electron energy distribution, we see corresponding changes (such as flares) in the emitted X–rays. From the energy dependence of these variations, we can infer constraints on the time scales for acceleration, injection, and cooling, and on the size of the synchrotron-emitting region. Adding two more blazars to the data already obtained for Mrk 421, we have a well-studied sample of three

TeV blazars, from which we can begin to study the range of properties of blazar jets.

We describe the *ASCA* observations and data reduction in § 2. In § 3, we discuss the analysis of the time series via the structure function method; this includes simulation of light curves as consisting of series of "shots." We compare the structure functions calculated for the observed and simulated data in order to verify what are the preferred parameters of such "shots." We discuss the variability time scales in § 4, address the question of the energy dependence of temporal variability through cross-correlations in § 5, and present our conclusions in § 6.

2. OBSERVATIONS AND DATA REDUCTION

We observed Mrk 421 for 7 days with *ASCA* in 1998 during April 23.97 – 30.8 UT, and for 10 days each of Mrk 501 and PKS 2155–304 during 2000 Mar 1.50 – 11.00 UT and 2000 May 1.55 – 11.50 UT, respectively. For all observations, the SIS (Solid-state Imaging Spectrometer; Burke et al. (1991); Yamashita et al. (1997)) was operated in 1 CCD FAINT mode for the high data rate, and BRIGHT mode for the medium/low rate. In order to combine with the BRIGHT mode data and apply standard data analysis procedures, the FAINT mode data were converted to BRIGHT mode data. Similarly, the GIS (Gas Imaging Spectrometer; Ohashi et al. (1996)) was always operated in the PH-nominal mode.

All data reduction was performed using the HEASOFT 5.0 software package. The screening criteria for both the SIS and GIS included rejection of data during passage through the South Atlantic Anomaly and for geomagnetic cutoff rigidity lower than 6 GeV/c. For the SIS, we used regions with angle from bright Earth greater than 20°, and angle from night Earth larger than 10°. We also selected only the X–ray events according to how the charge was distributed to the CCDs, namely these corresponding to grades 0, 2, 3, and 4. For the GIS, we accumulated data for bright Earth and night Earth elevation angles larger than 5°.

Source photons were extracted from circular regions centered at the target, with $3'$ and $6'$ radii for SIS and GIS, respectively for Mrk 501 and PKS 2155–304. As described in Takahashi et al. (2000), we use only the SIS for Mrk 421 since the source was sufficiently bright that there was telemetry saturation in the GIS. We used photons only from the smaller regions, corresponding to $1'$ and $2'.6$ radii for SIS0 and SIS1, respectively, in order to avoid saturation in the SIS cameras. The background data were examined using source-free regions in the same image. Because the background count rates and their fluctuations were negligible (less than 2 % at most), we did not perform any background subtraction before further analysis, so as to avoid introducing any artifacts. For the X–ray light curves, we combined as much data as feasible (i.e. 2 SISs for Mrk 421 and all SIS and GIS for the other two sources) to maximize the signal-to-noise ratio in each temporal bin.

2.1. Mrk 501

When the 10-day observation of Mrk 501 started, the object was in a moderately faint state, with its 2 – 10 keV flux at $\sim 6.0 \times 10^{-11}$ erg cm^{-2} s^{-1}, compared to an historical range of $\sim (1-60) \times 10^{-11}$ erg cm^{-2} s^{-1}(Della Ceca et al. 1990; Pian et al. 1998). The spectra integrated over short time periods were well fitted by power laws with photon index $\Gamma = 1.8 - 2.2$, well within the range previously observed. The spectrum indices suggests that the synchrotron peak is shifting over a wide range, from below to above the *ASCA* bandpass, during our observation.

The 10-day light curve is shown in Figure 1, where the heavy points represent the soft X–ray band (0.6 – 2 keV), and the light points represent the hard X–ray band (2 – 10 keV) in 5678 sec bins, equal to the satellite orbit period during the observation. Each light curve was normalized to its mean. After 2 days of small variations, there was a large flare, followed by 2 additional well-defined flares, and a further rise at the end of the observation. Even between the large flares there is additional, significant variability, so that Mrk 501 is never in a truly quiescent state. The amplitude of variability in the hard X–ray band is clearly larger, indicating a hardening of the spectrum during high states. The flares in the two bands are well correlated. In particular, near the maximum of the flare, there are apparently no lags larger than a few temporal bins (i.e., lags $\lesssim 10^4$ s).

Examining each flare in more detail, we observed that none of the large flares show a smooth rise or decay but exhibit substructures, with smaller flares having shorter time scales. This is demonstrated in the small panel which shows a blow-up of the last flare (marked with an arrow), where the hard energy band light curve is binned to 2048 sec. The overlapping, or closely placed flares are clearly resolved, and the rise and decay time scales are of the order of 5 – 10 ks. The amplitude of the substructures are equal to or larger than 10 %. We remark that in *ASCA*, and in particular in our case where the background level is less than 2 % throughout the observation, the statistical error completely dominates the systematical error, and thus the substructures cannot be due to background fluctuation etc.

All the large flares have different durations ranging from 40 to 100 ks, but importantly all flares have nearly symmetric time profiles, similar to those seen in the long-look observation of Mrk 421. The new result is that the substructures, lasting on the order of 5 – 10 ks, also all appear to be rather symmetric; no faster rise or decay than that time scale is apparent. However, the complicated superposition of flares makes it hard to make a quantitative statement regarding the symmetry of each flare. Further analysis regarding the symmetry using higher order moments will be presented in a separate paper.

2.2. PKS 2155–304

The observation of PKS 2155–304 also started with the source in a relatively faint state, with its 2 – 10 keV flux at $\sim 3.0 \times 10^{-11}$ erg cm^{-2} s^{-1}, compared to the historical range spanning $\sim (1.5 - 25) \times 10^{-11}$ erg cm^{-2} s^{-1}(Della Ceca et al. 1990; Kataoka et al. 2000). The time-resolved spectra, integrated over short time periods, were again well fitted by power laws with photon indices ranging $\Gamma = 2.5 - 2.8$, consistent with previous observations. Here the synchrotron peak must be below $\sim$ 1 keV, and the observed X–rays represent the high-energy tail of the electron energy distribution.

The *ASCA* light curve of PKS 2155–304 is shown in Figure 2. Again, the heavy points represent the soft X–ray band (0.6 – 2 keV), and the light points represent the hard X–ray band (2 – 10 keV), in 5657 sec bins. Each light curve was normalized to its mean. In this case, the intensity increased strongly towards the end of the observation, by nearly a factor of 3. This high amplitude is consistent with the steepness of the spectrum since we expect stronger variability above the synchrotron peak, where radiative losses dominate (if the peak represents an equilibrium between loss and acceleration processes).

In addition, there is continuous flaring throughout the 10-day observation, each having amplitude $\sim$ 30 – 50 %. Here the variability amplitudes in the hard and soft X–ray bands are very similar, indicating only a modest spectral change even during the large amplitude flare. The variability in the two energy bands is well correlated, and again concerning the flare maximum, any lags between the two bands must be smaller than $\sim 10^4$ sec.

A close look at the light curve again shows substructures present in the large flares. This can be seen in the small panel which shows a blow-up of the last part of the flare, using a 2048 sec binned light curve. Shorter variability with rise and decay time scales of $\sim$ 10 ks is clearly seen.

2.3. Mrk 421

The full 7-day light curve of Mrk 421 is shown in Figure 3. The heavy points represent the soft X–ray band (0.6 – 2 keV), and the light points represent the hard X–ray band (2 – 10 keV), in 5740 sec bins. Each light curve was normalized to its mean. This was the first TeV blazar where repetitive daily flares were observed. Details of the daily flares in Mrk 421 are presented in Takahashi et al. (2000).

The remarkable brightness of the source during the observation enabled us to further study the structure of the light curve in 512 sec bins. And for this source as well, the large daily flares clearly show substructures, as shown in the smaller panel. The time scale seems to be even shorter in Mrk 421 than in the other two objects, and the shortest flares that can be detected show significant variations with time scales of $\sim$ 5 ks.

3. STRUCTURE FUNCTION ANALYSIS

3.1. Structure Functions Derived from Observations

The continuous coverage and long duration of the *ASCA* observations provide the best opportunity to date for studying variability in blazars, enabling us to track the individual flares as well as the underlying component, and to determine the rise or decay time scales. However problems still remain since it is always difficult to unambiguously determine from the light curve whether a given observed flare is a single shot, or if it consists of shorter overlapping shots.

Another advantage of continuous long observations is that it is possible to employ the structure function, which can provide a quantitative statistical test of the time series. We use the formalism described in Simonetti, Cordes, & Heeschen (1985); one modification is that since photon statistics dominate the error in X–ray data (i.e. error depends on flux, unlike low frequency observations where systematic error dominates), we use a continuous weighing factor proportional to its significance of each data point instead of taking only either 0 or 1 as in Simonetti, Cordes, & Heeschen (1985). The definition of the 1st order structure function for a light curve described as $f(i)$ is then,

$$D_f^1(k) = \frac{1}{N^1(k)} \sum w(i)w(i+k)[f(i+k) - f(i)]^2, \tag{1}$$

where

$$\begin{aligned} N^1(k) &= \sum w(i)w(i+k), &(2)\\ w(i) &\propto \frac{f(i)}{\sigma_f(i)}. &(3) \end{aligned}$$

Here, $w(i)$ is the weighing factor, and $\sigma_f(i)$ is the 1 σ uncertainty of the data point $f(i)$ in the light curve. The summations are made over all pairs.

We set the light curve bin-size equal to the orbital period as used in Figure 1–3, so as to minimize the effect of short gaps mainly due to source occultation and passage through the SAA or high particle background regions. The orbital period was 5740.5 sec for Mrk 421, 5678.3 sec for Mrk 501, and 5657.2 sec for PKS 2155–304. The decrease of the orbital period in 10 days is short, no more than $\sim$ 5 s, and thus it is not taken into account. The calculated structure functions for the three sources are shown in Figure 4(a)–(c). We must remark that the "wiggling" feature at the longest time scales are due to the finite number of flares that exist in the observed light curve, and thus are not intrinsic to the source. The number of pairs in the summations in equation (1) decreases as the time difference increases, and accordingly the uncertainty becomes larger (see Kataoka et al. 2001 for a detailed discussion).

The first remark is the steep slope at the short time scales in all sources. The slope β of a structure function is believed to be an indicator of the nature of the intrinsic variation of the source; e.g. $\beta = 1$ for red noise (random walk), $\beta = 0$ for white noise. The slope at the shortest end of the separation time, $\beta \sim$1.5 for Mrk 501, $\beta \sim$1.4 for PKS 2155–304, and $\beta \sim$1.4 for Mrk 421, are all steeper even than the "random walk" case, meaning there is a rapid decrease in variability amplitude with temporal frequency. Somehow the variable source retains a "memory" of its state over a certain period. Another remark is the flattening of the slope at longer time scales, indicating little increase in variability amplitude. The observed breaks (characteristic time scale) are at ~ 1 day for Mrk 501, $\sim 2-3$ days for PKS 2155–304, and ~ 0.5 day for Mrk 421 (the second would be determined more precisely with a longer observation).

3.2. Simulated Light Curves and Structure Functions

The structure function analysis suggests that for all TeV blazars these functions have common features, a steep slope on the short time scales which flattens at longer time scales. On the other hand, it is not obvious what exactly these slopes and breaks indicate. The likely time scales to contribute would be the rise and decay time scales of each flare, and also the separation of the flares. Here we simulate various light curves and calculate the structure function in order to determine which parameters are most likely to affect the slopes and break time scales measured in the structure functions derived from the data.

In simulating the light curves, we regard the whole light curve as a superposition of various flares or "shots" occurring randomly, following a Poisson distribution. (An offset component is also possible, but this has no effect on the structure function.) The shape of each shots is difficult to determine from observation, but here we assume an simple triangle shape, where $\tau_{\rm r}$ is the rise time scale, $\tau_{\rm d}$ is the decay time scale, and $t_{\rm p}$ is the time of occurrence of the shot. With this,

$$f(t) = \begin{cases} A\,(t-(t_{\rm p}-\tau_{\rm r})) & \text{for } t \le t_{\rm p} \\ -A\,(t-(t_{\rm p}+\tau_{\rm d})) & \text{for } t > t_{\rm p}. \end{cases} \tag{4}$$

We note that the results obtained in the following sections concerning the slope and the location of the break time scale did not change if we instead assumed a Gaussian or an exponential time profile.

3.2.1. Dependence on τ

First, we consider the case where all shots have the same time scales $\tau_{\rm r} = \tau_{\rm d} = \tau$. We set τ=10 and 100, and simulated 2000 steps as the light curve, respectively. The shots occur randomly, with the average number of shots being 1 per time unit. The intensity of each shot is also set randomly, but the number density follows a power law distribution $N \propto A^{-1.5}$, where A is the normalization from equation (4). This distribution was chosen to be similar to gamma–ray bursts (Pendelton et al. 1996), but this again is not sensitive to the slope and break time scale of the resulting structure function. This will be used commonly throughout this section.

A set of simulated light curves for $\tau = 10$ and $\tau = 100$ are shown in Figure 5 (a-1) (a-2), and the calculated structure functions are shown in the top panel of Figure 6(a). The shape is similar to that calculated from the observations; a steep index at the short time scales and a flattening at longer time scales. The location of the break is clearly seen to shift together with the time scale of the individual shots in each light curve. The bottom panel shows the power-law index of the structure function, where we can see that the index of the steep slope reaches β=2 at the shortest time scale, and continuously flattens to β=0 towards the time scale τ.

3.2.2. Dependence on Rate

In the second case we fixed $\tau = 50$, and varied the average number of shots per time unit $R = 0.1$, 1, and 10. It is often the case that the variability amplitude of blazar flares is of the same order as the offset-like underlying component. It is not yet understood whether this is due to a flaring component superposed on a steady emission component (which requires continuous acceleration), or many flares generating the offset component. In fact, as can be seen in the simulated light curves for each case shown in Figure 5 (b-1) (b-2) (b-3), when the rate is set high, the visible flare amplitude becomes comparable to the underlying offset.

The resulting structure function and the index of the slope is shown in Figure 6(b). Here, only the normalization is changed, and the break remains at the same time scale not depending on the shot cycle. The steep slope reaching β=2 is also common.

3.2.3. Simulations with Variable τ

Now we consider a range of τ for individual shots. Figure 6(c) is the resulting structure function when τ takes a random value between $\tau_{\rm min} = 10$ and $\tau_{\rm max} = 100$. The rate is set to $R = 1$. The structure function of the case with a single $\tau = 100$ is also plotted for comparison. The steep slope $\beta \sim 2$ at the shortest time scale is similar to the case of a single τ, but it becomes flatter after $\tau_{\rm min}$, and becomes completely flat after $\tau_{\rm max}$. The slope between $\tau_{\rm min}$ and $\tau_{\rm max}$ is $\beta \sim 1$, The simulated light curve is shown in Figure 5(c-1),

3.2.4. Non-symmetric Shots

The last case considered by us is when the rise and decay of the individual shots are different. We fixed the decay time scale $\tau_{\rm d}$=100 and varied the rise time scale $\tau_{\rm r} = 1$, 10, and 100. The rate is set to $R = 1$. The simulated light curves are shown in Figure 5(d-1)(d-2), and Figure 6(d) is the resulting structure function. The time scale where the structure function completely flattens to $\beta = 0$ is common in all cases, but the slope in shorter time scales appears to vary. This is, however, exactly analogous to the above case where $\tau_{\rm r} = \tau_{\rm d} = \tau$ had a range. The index becomes 2 below the shortest τ and rises with $\beta \sim 1$ up to the longest τ. Since the observed light curve imposes a limit on the detectable shortest time scale, the observed slope in the structure function is consistent with a range of β. Accordingly, the steepest slope observed appears to be determined by the relation of the minimum observable time scale and the shorter time scale of the rise or decay.

3.3. Summary of the Simulations and the Detection Limit with the Structure Function

The results derived in the simulations above can be summarized as below. We recall that the assumption is that the whole variation (besides a DC component) is a result of randomly occurring "shots" superposed on each other.

1. The time scale of the individual shots τ determines the location of the break in the structure function, where the power-law slope approaches $\beta \sim 2$ towards the shorter time scale.
2. Result (1) doesn't depend on the shot occuring rates.
3. When τ takes a range of time scales, the break (from index of 2) occurs at the minimum time scale of those shots.
4. When the rise and decay time scales of the shots are different, the break occurs at the time scale that is shorter of the two.

The above considerations imply that when there is a minimum time scale τ for individual shots, the slope of the structure function becomes steep below τ, and approaches $\beta \sim 2$. For the longer time scales, the structure function increases up to where there is no more shots having that time scale.

On the other hand, it is also true that the structure functions are by definition being dominated by shots with larger amplitude. We tested this with adding very small amplitude and shorter time scale shots having $\tau = 10$ on top of a light curve with a single $\tau = 100$ as discussed above. A portion of the light curve is shown in Figure 7(a) and (b). Although the structure functions consisting of shots with individual values of τ would depend on τ as in Figure 6(a), the structure function of the summed light curve is very close to the one with only the larger long shots. Thus if there is a situation where there are numbers of very short shots having very small amplitude, together with a longer and larger amplitude variation, such small, rapid shots will not affect the structure function.

The situation would be the same when the time scale of the shots decreases with amplitude. Such a case can be envisioned if the electron density is equal for each emission region in the jet: the region size would then be smaller for smaller shots. Thus the important result is that it is that we cannot reject the existence of a variable component having shorter time scales than the break time scale, but such a component, which would be characterized by short time scale, cannot dominate the variability in the light curve.

4. DISCUSSION OF THE TIME SCALES

The long look observations of TeV blazars showed that daily flares are common to all sources, and that there was actually no particular quiescent period throughout our observations. The observation of Mrk 501 and PKS 2155–304 in 2000 caught the sources in relatively faint states compared to the historical values of their flux, which also demonstrated that a high state is not a requirement for rapid variability. Another important result is that each of the day-scale flares is actually not a single, isolated flare, but shows substructures with shorter time scales of $\sim 5 - 10$ ks. This was observed commonly in our long-look observations for all sources. We will further discuss this short time scale variability at the end of this section.

Structure function analysis showed that the X–ray light curves of all TeV blazars have two common features: a very steep slope at the shortest time scale (steeper than red noise), and a break at the time scale of $\sim$ a day, where the slope flattens toward longer time scales. As shown from the simulations above, the location of this break (where the slope turns over from a power-law index of $\beta = 2$), is indicative of time scales characteristic of individual flares. The observed steepest power-law slope at the shortest time scales was $\beta = 1.5$, 1.4, and 1.4 for Mrk 501, PKS 2155–304, and Mrk 421, respectively. This slope is likely to reach the value of $\beta = 2$ at even shorter temporal frequencies. In fact, we derived a steeper slope at even shorter time scales by using a light curve in shorter time bins, $\beta \sim 1.8$ for Mrk 421; probing these shorter time scales in Mrk 501 and PKS 2155–304 becomes more difficult since the photon counts are smaller, and the effect of the measurement error cannot be completely removed.

Estimating the exact location of the break requires careful simulations as described in Kataoka et al. (2001), but the important result here is the existence of a common break in the structure functions. This was suggested in Kataoka et al. (2001) by collecting all previous *ASCA* and *RXTE* observations up to 1999. However, an actual confirmation of this suggestion required a single, continuous, long-look observation in the X–ray range, which we presented above.

Another observational result from the *ASCA* long looks at TeV blazars in the X–ray band is that the flares are always nearly symmetric. This is often interpreted by the light-crossing time dominating the variability time scale and thus smearing out the other time scales (Chiaberge & Ghisellini 1999). In our simulations where the time series consists of superposition of individual "shots," the characteristic time scale in the structure function is likely to reflect the time scales of the individual shots: with this, the light-crossing times are most likely to determine the characteristic time scale in the structure functions. Furthermore, because the flares do not have flat-top profiles, this suggests that the cooling and acceleration time scales are comparable to the light-crossing time. The cross-correlation analysis given below showing significant lags of both signs (soft-lags and hard-lags) also supports the inference that the cooling and acceleration time are comparable.

The cooling time (in the observer's frame) of the electron emitting synchrotron photons with energy $\mathrm{E_{keV}}$ can be calculated as $\tau_{\rm cool} \simeq 1.7 \times 10^4 \, (1 + u_{\rm soft}/u_{\rm B})^{-1} \, \delta_{10}^{-0.5} \, B_{0.1}^{-1.5} \, E_{\rm keV}^{-0.5}$, where $B_{0.1}$ is the magnetic field in units of 0.1 Gauss, and δ_{10} is the beaming factor in units of 10. Here the peak frequency of the synchrotron spectrum is given by $\nu \sim 1.2 \times 10^6 \, B \, \delta \, \gamma^2$. (e.g., Rybicki & Lightman 1979). Fitting the multi-frequency spectra, Kataoka (2000) derived the magnetic fields B and beaming factors δ of respectively $B = 0.13$ Gauss, $\delta = 14$ for Mrk 421, $B = 0.13$ Gauss, $\delta = 9$ for Mrk 501, and $B = 0.14$ Gauss, $\delta = 28$ for PKS 2155–304. With this, we infer the cooling times for the electrons corresponding to 1 keV photons to be $\sim$ 5000, $\sim$ 6000, and $\sim$ 3000 s, respectively. Although some flexibility still remains in these model parameters, and even considering that all parameters may change by a factor of 2 (Tavecchio, Maraschi, & Ghisellini 1998; Kataoka et al. 1999; Kataoka 2000), the cooling time is likely to fall in the range of $1 - 10$ ks. Also because these parameters were derived for different epochs, they may not be exactly identical during the flares observed in the long look observations. However, given the fact that the values derived for various epochs are not that different, it is natural to think that the parameters during our observations are quite similar to the values given above. Thus, assuming that the observed characteristic time scale (i.e. $\sim$ a day) is reflecting the light-crossing time of the emission region, this calculation indicates that the cooling time of the electrons emitting the X–ray photons is significantly shorter than the light crossing time.

The origin of flares observed in blazars is far from being fully understood, but one of the simplest scenarios would be an increase in the numbers of electrons injected into the acceleration region. This may well be a region where a shock is passing through some region where the electron density is high (e.g. Kirk, Rieger, & Mastichiadis 1998). These electrons will escape from the acceleration process and enter the emission region and cool. In this scenario, the overall emission region would be defined by the size of the region where the number of injected electrons is high. Furthermore, if this emission region has a size characterized by a time scale of $\sim$ a day, the number of injected electrons is unlikely to be constant since the cooling time of the electrons is short. With this, in order to have a flare without a flat-top when the acceleration and cooling times are much shorter than the light-crossing time, it is likely that electron density is somewhat inhomogeneous, and/or it is an effect of a more complex geometry (such as a sphere, instead of a shell with constant thickness).

One of the important observational results discovered in our long-look observations is the common existence of substructures, having shorter variability time scales, on the order of $\sim$10 ks (hereafter referred to as '$\sim$ 10 ks flares'), apparent via closer examination of the larger day-scale flares in the observed light curve. This was also observed in the recent light curve of Mrk 421 taken by the *XMM-Newton* satellite which showed with great statistics overlapping flares with time scales of $\sim 5 - 10$ ks (Brinkmann et al. 2001). It is not obvious whether these $\sim$ 10 ks flares are superposed on a longer and larger amplitude flare, or if the entire variability is a result of a superposition of a number of these $\sim$ 10 ks flares piled up on top of each other. If individual shots are to have this time scale of $\sim$ 10 ks, reflecting the light-crossing time, the cooling and acceleration times would be in good agreement with the light crossing time, which would be in turn consistent with the observed symmetric non-flat-top flares.

Our simulations showed that if the entire variability consists of shots with time scales of 10 ks occurring randomly, a break in the structure function (indicating the characteristic time scale) will be located at 10 ks (see Figure 6). Even if such time series consisted of a mixture of shots having randomly distributed time scales with a minimum at 10 ks, the location of the break will still be at 10 ks. However, as was shown in Figure 4, observations definitely show a characteristic time scale at $\sim$ a day. This implies that if all shots have the time scale of 10 ks, the occurrence of such shots should not be fully random, but by somehow correlated with each other, generating the observed characteristic time scale of $\sim$ a day. This can be either correlated in time, or in space.

If shots with longer time scale also exist, there must be a reason for the shorter shots having smaller amplitude than the longer ones, since otherwise, the break time scale in the structure function would be located at 10 ks. Small variations superposed on the larger flares having the characteristic time scale may also be a likely explanation. Our *ASCA* observations do not have enough statistics to fully resolve and study the energy dependent variability in the smaller flares. Continuous monitoring with telescopes with larger photon collecting area, such as *XMM-Newton*, would surely help further understandings of the shorter time scale variability.

5. CROSS CORRELATION AND LAGS AS A FUNCTION OF ENERGY

The goal of X–ray monitoring of blazars is to understand the underlying jet physics. The time scales of variability and spectral changes across flares can be interpreted in terms of the time scales for electron injection, acceleration, and cooling, taking into account propagation of light across the emitting volume and from the source to us. For example, soft lags, i.e. the hard energy band leading the variation, have been interpreted as signatures of synchrotron cooling (Tashiro 1992; Takahashi et al. 1996; Urry et al. 1997; Kataoka et al. 2000). Intensive X–ray monitoring of blazars has revealed not only soft lags but in some cases hard lags (Sembay et al. 1993; Takahashi et al. 2000; Catanese & Sambruna 2000), which may be interpreted in terms of the energy dependence in acceleration time scales. The physical situation is likely more complex than assumed in the simple cooling scenario.

To explore further the energy dependence in the variability than is readily apparent from the light curve in Figure 1–2, we make use of the discrete correlation function (DCF) method developed by Edelson & Krolik (1988) and also the modified mean deviation (MMD) method originally introduced by Hufnagel & Bregman (1992). The advantage of the DCF compared to the classical correlation function is that it is applicable to unevenly sampled data, thus only the existing data are used, requiring no interpolation. For the calculations we binned the light curve in bin sizes of 1024 s.

We must remark that "lags" studied in this paper do not necessarily indicate one energy band being a delayed version observed in the other band. This is rather different from situations of comparing 2 time series where one is thought to be driven by the other, such as the lines and continuum (e.g. Edelson & Krolik 1999; Vaughan & Edelson 2001) or thermal reprocessing (e.g.

Edelson et al. 1996; Nandra et al. 2000) in Seyfert galaxies. The time series we are comparing here are certainly due to the same electron population cooling via a common radiation process; in our case, this is primarily synchrotron emission, where the rate of electron energy loss is dependent on that energy. (Compton cooling for this energy range of electron is strongly suppressed by the Klein-Nishina cutoff. e.g. Kataoka 2000; Li & Kusunose 2000) If cooling or acceleration is the cause of lags as it is often interpreted, the difference is likely to arise in the decay or rise time scales of the flares, and what we want to verify and quantify is the energy dependence. In this case, the DCF or MMD is likely to be asymmetric indicating the differences of the time scales, and the deviation from zero lag is still useful to parameterize the energy dependence of the time scales. After investigating the cross correlations, we comment on the importance of evaluating the significances of the values of the lags.

5.1. Analysis of Complete Time Series

We first considered the full light curve data sets. We separated each light curve into 4 energy bands, 0.6 – 1.2 keV, 1.2 – 1.8 keV, 1.8 – 3 keV, and 3 – 10 keV, and calculated the DCF/MMD of the lower three energy bands against the 3 – 10 keV band. The case of comparing of the 0.6 – 1.2 keV and 3 – 10 keV data is shown in the middle and bottom panels in Figure 8 for all three sources. We can see that there is strong correlation with $r_{\rm max} \geq 0.8$ for all sources. Here, $r_{\rm max}$ is defined by the maximum of the correlation peak. In contrast to the common strong correlation, the width of the correlation peak appears different in each source, with PKS 2155–304 being the widest of the three. This comes from the fact that cross-correlation functions are convolutions of autocorrelation functions with non-zero width. This can be seen by comparing with the autocorrelation functions (ACFs) measured using the DCF technique shown in the top panels of Figure 8. The width of the ACF peak is smallest in Mrk 421 ($\sigma \sim 15$ ks, when fitted with a Gaussian function), second in Mrk 501 ($\sigma \sim 30$ ks), and largest in PKS 2155–304 ($\sigma \sim 60$ ks). In the previous sections, we argue that all TeV blazars have a characteristic time scale which is likely reflecting the time scales of the day-scale flares. It is interesting to note that the characteristic time scales derived in the structure function analysis in section 3, are commonly 2–3 times of the width (defined as the σ as above) of the ACF peak.

We estimated the lag by fitting a Gaussian plus constant model (see discussions in Edelson et al. 1995; Peterson et al. 1998) to each DCF and MMD. The results of the energy dependent lag for the three sources are presented in Table 1. The positive value indicates the soft band lagging the hard band. Here, PKS 2155–304 was the only source to show a soft lag with the "expected" energy dependence, increasing value with larger energy gap. There was no evidence of lags using the entire light curve in the Mrk 421 or Mrk 501 data (consistent with no lag within the statistics). The errors represent the 1 σ uncertainty estimated by realistic Monte-Carlo simulations, using mainly the flux randomization (FR) and random subset selection (RSS) methods described in Peterson et al. (1998). All uncertainties concerning lags will be estimated in the same way throughout the paper.

5.2. Analysis of Individual Flares

Following the examination of the entire time series, we also studied individual flares. Here we restrict our discussion to the flares with the rise and decay times on the order of the characteristic time scale of the source derived from the structure function analysis, thus the time scale dominating the variability power (i.e. the day-scale flares, not the small hour-scale substructures). The results for Mrk 421 during the long-look campaign are described in Takahashi et al. (2000), and thus here we only discuss in detail the results for Mrk 501 and PKS 2155–304. For Mrk 501 this was straightforward, since the light curve can be divided clearly into segments spanning each of the first three large flares, and the rise part at the end. Regarding the time regions we took the data corresponding to the running time of the observation of 160 – 340 ks, 440 – 520 ks, and 570 – 600 ks, and we refer to those respectively as flare1, flare2, and flare3. The calculated DCF and MMD between the 0.6 – 1.2 keV and 3 – 10 keV band for each flare are shown in Figure 9. Again, the lag was first estimated by fitting a Gaussian plus constant model. This is shown as the solid line in Figure 9. The results of the energy dependent lag for the three flares are summarized in Table 2(a). Interestingly, in contrast to the full light curve of Mrk 501 which showed no detectable lag, the individual flares had different features. Flare1 showed a soft lag, and flare2 a hard lag, although the significance is small for flare1 (2.5 σ for the lowest and highest energy band). Flare3 also shows a trend of a soft lag, but the significance is also small. The values of the lags are in the range of $\sim 1 - 10$ ks, which is $\lesssim 2$ bins of the counts light curves plotted in Figure 1.

The flares in PKS 2155–304 are more complicated (with overlapping smaller flares), but concentrating on the flares dominating the variability power, we divided the light curve into 3 time regions, 0 – 200 ks, 200 – 500 ks, and 500 – 840 ks (referred to as flare1, flare2, and flare3, respectively). The calculated DCF and MMD for the 1.2 – 1.8 keV and 3 – 10 keV bands for each flare are shown in Figure 10. Similarly, lags were estimated by fitting a Gaussian plus constant model as shown together as solid lines. The results of the energy dependent lag for the three flares are summarized in Table 2(c). Here, flare1 and flare2 showed a energy dependent soft-lag, where no detectable lag was seen in flare3.

In several ACFs such as in flare2 of Mrk 501 in Figure 9(b), a sharp peak around zero-lag is clearly seen. This is most likely due to the “correlated error”, which can generate a zero-lag peak in the DCF or MMD as well, when the compared two time series are obtained from a single set of observations. However, as pointed our by Peterson et al. (1998), the artificial correlation at zero-lag due to correlated errors would drive the measured cross-correlation lags to smaller values. Thus, even if correlated errors were to affect the data, our results would have been a conservative estimate of the significance of a inter-band lag larger than zero.

5.3. Uncertainties in the Lags

As discussed in Edelson et al. (2001), there are concerns about measured lags that are smaller than the orbital periods in low-Earth orbit satellites. Periodic interruptions are generated due to the Earth occultation, and the orbital period is 5.6 – 5.8 ks, comparable to the measured lags. However, as can be seen from the histograms of the DCF or MMDs, the whole peak (determined from the width of the auto-correlation) is shifted, or is asymmetric, showing more correlation on one side than the other, and there is no simple instrumental or sampling reason for this. We emphasize again that the flares we are considering are the ones that have the time scales which are quite similar to the characteristic time scales which dominate the variability. Another important fact in the case of *ASCA* data is that the time series in different energy bands are all taken by the same set of instruments (2 GISs and 2 SISs) so that the observing periods are *exactly* simultaneous. Accordingly, the data gap in the DCF or MMD peak is symmetrical with respect to the zero lag, and thus there is little chance to measure an artificial lag from time series with truly zero-lag. Thus we conclude that there is little effect of the orbital gap on the measured lags.

Another concern about the significance of the lags is the effect of the underlying component. For instance, if a flare is located on top of a rising underlying component, the peak of the flare would appear to be delayed in time. And if this increase is relatively steeper (i.e. as compared to the amplitude of the flare in its energy band) for the soft energy band, an erroneous soft lag will be inferred if the offset component is ignored. From the structure function analysis using data sets covering longer time spans, we know that there is variability on time scales up to years in blazars (Kataoka et al. 2001), and thus a reliable measurement of inter-band lags for a specific flare requires that the offset component is subtracted.

We tested this for the Mrk 501 data, where the flares are clearly separated and the offset is rather well defined. This correction was not possible for previous data, where the typical observation times were $\sim$ a day and the long-term trend couldn't be reliably established. We first estimated the underlying component by fitting the light curve on both sides of the flare with a linear function for each energy band. We then calculated the lags in the same manner as above, after subtracting the underlying component. The result is shown in Table 2(b), where the estimated value of the lag became smaller, but there is still a significant lag for flare1 and flare2. Since the shape of the underlying component is not determined unambiguously, we also attempted modeling the offset with a second order polynomial and an exponential, but the lag remained. In summary, although there is still possibility that the measured lags are artificial due to the underlying component which we cannot determine exactly, we conclude that assuming a simple linear offset, the lag is real. A follow up discussion for the lags inferred previously from the *ASCA* data for Mrk 421 (Takahashi et al. 1996) and PKS 2155–304 (Kataoka et al. 2000) is given in Appendix A.

Another important result is that inter-band lags are *not* universal. From the multiple flares detected in the long look observations, we showed that the energy dependence of the lags can differ from flare to flare. This supports the indication inferred for Mrk 421 (Takahashi et al. 2000) that in

TeV blazars, the intrinsic variability time scales including acceleration and cooling of the electrons radiating in the X–ray range are comparable, and that the balance of these parameters controls the observed lags.

6. SUMMARY AND CONCLUSIONS

We have conducted a unprecedented, uninterrupted long-look X–ray observations of the 3 brightest TeV Blazars, namely Mrk 421, Mrk 501, and PKS 2155–304. The last two observations made use of the opportunity of the continuous long-look observations in the last phase (AO-8 program) of *ASCA*. All sources commonly show continuous strong X–ray flaring, despite the relatively faint intensity states in the last two sources.

Structure function analysis shows that all TeV blazars have a break in the structure function at a time scale of $\sim$ a day indicating a characteristic time scale, and a very steep slope below the characteristic time scale suggesting strong suppression of the more rapid variability. We carried out simulations in order to verify the sensitivity of the observed slope and break time scales to assumed parameters. In particular, we assumed that the time series consists of randomly occurring flares ("shots") superposed on each other and this results in the observed variability. With this, we inferred that the time scale of the break in the structure function indicates the minimum time scale of the individual shots, and the slope at shorter time scales than the break becomes steeper than 1 until it finally reaches 2. On the other hand, we also detected faster substructures having time scale of $\sim$ 10 ks, but with smaller amplitude which is consistent with those not affecting the structure function. The entire variability may also consist of such $\sim$ 10 ks shots, but if that were the case, in order to match the observations, we argue the shots should not be fully random but somewhat correlated with each other. The near-symmetry of the observed flares and the suppression of fast variability indicates that the characteristic time scale is determined by the light crossing time, and thus dominating the time scales of the day-scale flares. In this case, since the acceleration and cooling times of the electrons are calculated to be significantly shorter than the light-crossing time, an inhomogeneous electron distribution (or some other geometrical effect) is required in order to account for the non-flat-top flares.

The energy dependent cross-correlations suggest that inter-band lags are not universal in TeV blazars. From the multiple flares detected in the long-look observations, we showed that the energy dependence of the lags differs from flare to flare. This supports the inference that the time scales of acceleration and cooling of the electrons responsible for the X–ray emission are comparable for TeV blazars, and the balance of these parameters controls the lags. On the other hand, we pointed out that some uncertainties remain, mainly concerning the nature of the underlying component of variability on even longer time scales than considered here.

Support for this work was provided by the Fellowship of Japan Society for Promotion of Science for Young Scientists, and NASA through grant number GO6363.01-95A from the Space Telescope Science Institute, which is operated by AURA, Inc., under NASA contract NAS 5-26555. CT and GM acknowledge support from Smithsonian Astrophysical Observatory via SAO grant number GO0-1038A.

A. COMMENTS ON THE LAGS PREVIOUSLY MEASURED IN THE X–RAY DATA FOR MRK 421 AND PKS 2155–304

Here we provide a follow-up discussion concerning the significance of the the previously published analysis of lags on Mrk 421 and PKS 2155–304 (Takahashi et al. 1996; Kataoka et al. 2000). In similarity to the flares observed in the long-look observations, we separated the light curves into 4 energy bands corresponding to 0.6 – 1.2 keV, 1.2 – 1.8 keV, 1.8 – 3 keV, and 3 – 10 keV, and binned all light curves in 1024 sec bins. The DCF and MMD are calculated for the lower three energy bands against the 3 – 10 keV band, and the error is estimated by the same simulations (see text). The case of comparing 0.6 – 1.2 keV and 3 – 10 keV is shown in Figure 11. We can see that there is strong correlation for both sources with $r_{\max} > 0.95$, and that the whole cross-correlation peak is shifted to the positive side, indicating a soft-lag. The value of the lag is estimated as the peak value of a Gaussian fitting the correlation peak. The derived parameters including the other energy bands are summarized in Table 3. We also suggest that the low value of correlation ($r_{\max}$) of PKS 2155–304 in Zhang et al. (1999) pointed out by Edelson et al. (2001) is probably due to the fine binning of the light curve.

As described in the text, there are concerns about the underlying component, which was assumed to be constant in previous analysis. We tested this by assuming a linear underlying component with a positive inclination for the soft energy band light curve. We varied the relative amplitude from 0 to 100 %, subtracted it from the light curve, and calculated the cross-correlations against the 3 – 10 keV light curve. For the 3 – 10 keV light curve, we subtracted only a constant offset for simplicity. Figure 12 shows the measured lag between the 0.6 – 1.2 keV and 3 – 10 keV light curve as a function of the assumed percentage of the rise of the underlying component for both Mrk 421 and PKS 2155–304. As expected, it is clearly seen that the measured lag becomes smaller as the assumed inclination is higher, and that a rising component with an increase of ∼70 % for Mrk 421 and ∼60 % for PKS 2155–304 is needed to cancel out the observed lag. In other words, if there is an underlying component rising with an amplitude of 60 – 70 %, we will obtain the value of lag that we measured, when in reality no lag exists for the flare itself. On the other hand, it is likely that the hard energy band would also rise when the lower energy band rises, and accordingly this percentage is certainly a minimum value; thus at least 60 – 70 % rise is required to cancel out the observed lag. An underlying component increasing with such a large amplitude is not very often observed, but cannot be ruled out.

REFERENCES

Blandford, R. D., & Konigl, A. 1979, ApJ, 232, 34

Brinkmann, W., et al. 2001, A&A, 365, L162

Burke, B. E., et al. 1991, IEEE Trans. ED-38, 1069

Catanese, M., et al. 1997, ApJ, 487, L143

Catanese, M., & Sambruna, R. M. 2000, ApJ, 534, L39

Chiaberge, M., & Ghisellini, G. 1999, MNRAS, 306, 551

Chadwick, P. M., et al. 1999, ApJ, 513, 161

Della Ceca, R., Palumbo, G. G. C., Persic, M., Boldt, E. A., Marshall, F. E., & de Zotti, G. 1990, ApJS, 72, 471

Edelson, R. A., & Krolik, J. H. 1988, ApJ, 333, 646

Edelson, R. A., et al. 1995, ApJ, 438, 120

Edelson, R. A., et al. 1996, ApJ, 470, 364

Edelson, R. A., Griffiths, G., Markowitz, A., Sembay, S., Turner, M. J. L., & Warwick, R. 2001, ApJ, in press (astro-ph/0102458)

Hufnagel, B. R., & Bregman, J. N. 1992, ApJ, 386, 473

Kataoka, J., et al. 1999, ApJ, 514, 138

Kataoka, J., Takahashi, T., Makino, F., Madejski, G. M., Tashiro, M., Urry, C. M., & Kubo, H. 2000, ApJ, 528, 243

Kataoka, J., Ph.D Thesis, University of Tokyo

Kataoka, J., et al. 2001, ApJ, in press (astroph/0105022)

Kirk, J. G., Rieger, F. M., & Mastichiadis, A. 1998, A&A, 333, 452

Li, H., & Kusunose, M. 2000, ApJ, 536, 729

Macomb, D. J., et al. 1995, ApJ, 449, L99

Maraschi, L., et al. 1999, ApJ, 526, L81

Nandra, K., Le, T., George, I. M., Edelson, R. A., Mushotzky, R. F., Peterson, B. M., & Turner, T. J. 2000, ApJ, 544, 734

Ohashi, T., et al. 1996, PASJ, 48, 157

Pendelton, G. N., et al. 1996, ApJ, 464, 606

Peterson, B. M., Wanders, I., Horne, K., Collier, S., Alexander, T., Kaspi, S., & Maoz, D. 1998, PASP, 110, 660

Pian, E., et al. 1998, ApJ, 492, L17

Punch, M., et al. 1992, Nature, 358, 477

Quinn, J., et al. 1996, ApJ, 456, L83

Rybicki, G. B., & Lightman, A. P. 1979, Radiative Processes in Astrophysics (New York: Wiley)

Sambruna, R. M., et al. 2000, ApJ, 538, 127

Simonetti, J. H., Cordes, J. M., & Heeschen, D. S., 1985, ApJ, 296, 46

Sembay, S. et al. 1993, ApJ, 404, 112

Takahashi, T., et al. 1996, ApJ, 470, L89

Takahashi, T., et al. 1999, Astroparticle Physics, 11, 177

Takahashi, T., et al. 2000, ApJ, 542 L105

Tashiro, M., 1992, Ph.D Thesis, University of Tokyo

Tavecchio, F., Maraschi, L., & Ghisellini, G. 1998, ApJ, 509, 608

Urry, C. M., & Padovani, P. 1995, PASP, 107, 803

Urry, C. M., et al. 1997, ApJ, 486, 799

Ulrich, M. H., Maraschi, L., & Urry, C. M. 1997, ARA&A, 35, 445

Vaughan, S., & Edelson, R. 2001, ApJ, 548, 694

Yamashita, A., et al. 1997, IEEE Trans Nucl. Sci., 44, 847

Zhang, Y. H., et al. 1999, ApJ, 527, 719

This preprint was prepared with the AAS LaTeX macros v5.0.

Fig. 1.— X–ray light curve of Mrk 501 binned equally to the satellite orbital period during the particular observation. *heavy points:* soft X–ray band (0.6 – 2 keV); *light points:* hard X–ray band (2 – 10 keV). Each light curve is normalized to its mean count rate, i.e. 6.0, 3.4 cts/s, respectively. A blow-up of light curve during the time region between the arrow is shown in the box, which demonstrates the further rapid variability within the day-scale flares.

Fig. 2.— Same plot as Figure 1 for PKS 2155–304. The soft X–ray and hard X–ray light curve is normalized to its mean count rate, 7.0, 2.1 cts/s, respectively.

Fig. 3.— Same plot as Figure 1 for Mrk 421. The soft X–ray and hard X–ray light curve is normalized to its mean count rate, 17.6, 5.5 cts/s, respectively.

Fig. 4.— Structure functions for (a) Mrk 501, (b) PKS 2155–304, and (c) Mrk 421, calculated from the X–ray light curves. All TeV blazars appear to have structure functions with a steep rise at shorter time scales and a break at a characteristic time scale.

Fig. 5.— The simulated light curves at following conditions; (a) When all shots have a single time scale; τ = 10 (a-1) and 100 (a-2). (b) When all shots have a single time scale τ = 50, and the average rate of shots per time unit is varied: R = 0.1 (b-1), 1 (b-2), 10 (b-3). (c-1) When each shot is characterized by a random time scale varying from 10 to 100. (d) When the rise and decay time scale differ. The decay time scale is fixed to $\tau_{\rm d}$ = 100, and the rise time $\tau_{\rm r}$ = 1 (d-1), and to 10 (d-2).

Fig. 6.— Structure functions (top panel) and their power-law indices (lower panel) for the simulated light curves shown in Figure 3 under the following conditions: (a) When all shots have a single time scale τ. The crosses show the structure function for τ = 10, and the diamonds are for τ = 100. The former is multiplied by a factor of 10; the break position indicates the time scale of individual shots. (b) When all shots have a single time scale τ = 100, and the average rate of shots per time unit is varied. We can see that the break position does not change as a result of varying the rate. (c) When the shots have a random time scale varying from 10 to 100. The case with only τ = 100 is shown as crosses, multiplied by a factor of 10. (d) When the rise and decay time scales differ. The comparison is with the decay time scale fixed to $\tau_{\rm d}$ = 100, and the rise time $\tau_{\rm r}$ = 1, 10, and 100.

Fig. 7.— The effect of small amplitude short shots on the structure function. (a) a portion of the simulated light curve which consists of single time scale shots (τ = 100), and (b) with a small and short time scale (τ = 10) shots added on top. (c) The calculated structure function and its index from the light curve with and without the short time scale flares added. Because the structure function is dominated by larger amplitude variations, the shorter time scale component will not appear in the structure function.

Fig. 8.— The discrete ACF of the 3 – 10 keV light curve (top), and the DCF (middle) and MMD (bottom) between the 0.6 – 1.2 keV and 3 – 10 keV band calculated for the entire light curve are

shown for all three sources: (a) Mrk 501, (b) PKS 2155–304, and (c) Mrk 421. A positive time lag in the DCF and MMD plot indicates the 0.6 – 1.2 keV band delayed from the 3 – 10 keV band.

Fig. 9.— The discrete ACF of the 3 – 10 keV light curve (top), and the DCF (middle) and MMD (bottom) between the 0.6 – 1.2 keV and 3 – 10 keV band calculated for the individual flares in PKS 2155–304. A positive time lag in the DCF and MMD plot indicates the 0.6 – 1.2 keV band delayed from the 3 – 10 keV band.

Fig. 10.— The discrete ACF of the 3 – 10 keV light curve (top), and the DCF (middle) and MMD (bottom) between the 0.6 – 1.2 keV and 3 – 10 keV bands calculated for the individual flares in Mrk 501. A positive time lag in the DCF and MMD plot indicates the 0.6 – 1.2 keV band delaying from the 3 – 10 keV band.

Fig. 11.— The discrete ACF of the 3–10 keV light curve (top), and the DCF (middle) and MMD (bottom) between the 0.6 – 1.2 keV and 3 – 10 keV band calculated for the 1994 *ASCA* data of (a) Mrk 421 and (b) PKS 2155–304. A positive time lag in the DCF and MMD plot indicates the 0.6 – 1.2 keV band delayed from the 3 – 10 keV band.

Fig. 12.— The measured soft lag of the 0.6 – 1.2 keV band against the 3 – 10 keV band as a function of the assumed amplitude of the underlying offset component for Mrk 421 (filled circles) and PKS 2155–304 (open circles). It is shown that a increase with an amplitude of 50 – 70 % is needed to cancel out the obtained lag.

Table 1. Energy dependent cross-correlation results for the full light curve

	Mrk 421			Mrk 501			PKS 2155–304		
E^{a} (keV)	DCF $r_{\max}$	DCF peak^{b}	MMD peak^{b}	DCF $r_{\max}$	DCF peak	MMD peak	DCF $r_{\max}$	DCF peak	MMD peak
0.6-1.2	0.80	-1.85±0.76	-0.13±0.52	0.78	-0.06±0.83	-2.59±1.42	1.00	3.87±0.98	3.62±0.93
1.2-1.8	0.87	-0.66±0.42	0.23±0.26	0.87	1.02±0.56	-0.21±0.87	1.00	2.76±0.80	2.13±0.72
1.8-3.0	0.89	-0.11±0.26	0.30±0.15	0.90	0.68±0.47	0.26±0.62	1.01	1.44±0.64	1.37±0.48

[a] All results show the correlation calculated against the 3 – 10 keV light curve

[b] Positive values indicate the soft energy band lagging the 3 – 10 keV light curve in units of kiloseconds.

Table 2. Energy dependent cross-correlation results for the individual flares in Mrk 501 and PKS 2155–304

	Flare1			Flare2			Flare3		
E^{a} (keV)	DCF $r_{\max}$	DCF peak^{b}	MMD peak^{b}	DCF $r_{\max}$	DCF peak	MMD peak	DCF $r_{\max}$	DCF peak	MMD peak
(a) Mrk 501									
0.6-1.2	0.99	2.58±0.97	1.75±1.25	0.57	-8.64±2.00	-7.36±2.59	0.61	0.52±1.47	3.10±2.08
1.2-1.8	1.00	1.98±0.63	1.99±0.86	0.65	-5.60±1.74	-4.98±1.97	0.82	2.93±0.92	3.58±1.11
1.8-3.0	1.04	1.40±0.52	1.66±0.56	0.74	-3.27±1.37	-3.18±1.51	0.91	2.63±0.83	2.95±0.88
(b) Mrk 501 (linear offset subtracted)									
0.6-1.2	1.01	2.51±1.00	1.95±1.19	0.59	-5.85±1.84	-3.06±2.30	0.62	-1.22±1.43	0.90±1.91
1.2-1.8	1.02	1.50±0.64	1.67±0.81	0.70	-3.33±1.58	-2.04±1.58	0.85	1.97±0.83	2.44±0.95
1.8-3.0	1.06	0.82±0.54	1.21±0.57	0.77	-1.69±1.27	-1.41±1.16	0.93	1.95±0.75	2.16±0.78
(c) PKS 2155–304									
0.6-1.2	0.72	6.06±2.48	6.76±2.81	0.77	9.60±2.30	6.85±2.44	0.97	0.60±0.69	1.35±0.59
1.2-1.8	0.72	3.78±2.32	4.72±2.50	0.80	7.95±2.18	4.06±2.33	0.98	0.28±0.67	0.74±0.58
1.8-3.0	0.73	3.95±2.13	2.49±1.84	0.79	4.05±2.08	2.54±1.94	0.97	-0.20±0.59	0.73±0.48

[a] All results show the correlation calculated against the 3 – 10 keV light curve

[b] Positive values indicate the soft energy band lagging the 3 – 10 keV light curve in units of kiloseconds.

Table 3. Energy dependent cross-correlation results for the 1994 *ASCA* observation

	Mrk 421			PKS 2155–304		
E[a] (keV)	DCF $r_{\rm max}$	DCF peak[b]	MMD peak[b]	DCF $r_{\rm max}$	DCF peak	MMD peak
0.6-1.2	0.98	5.38±1.33	6.40±1.28	1.10	3.02±0.72	3.37±0.54
1.2-1.8	0.97	4.02±1.03	4.68±1.24	1.11	2.73±0.59	2.82±0.42
1.8-3.0	0.97	2.62±0.62	2.56±0.85	1.10	1.83±0.39	1.87±0.31

[a] All results show the correlation calculated against the 3 – 10 keV light curve

[b] Positive values indicate the soft energy band lagging the 3 – 10 keV light curve in units of kiloseconds.

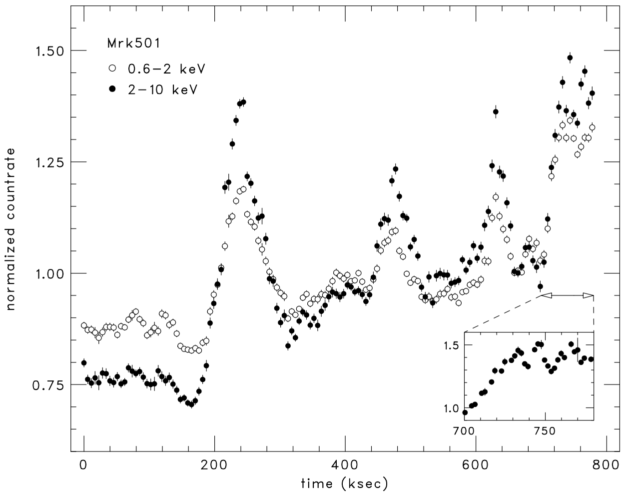
Mrk501
○ 0.6−2 keV
● 2−10 keV
normalized countrate
time (ksec)
0.75
1.00
1.25
1.50
0
200
400
600
800
1.0
1.5
700
750

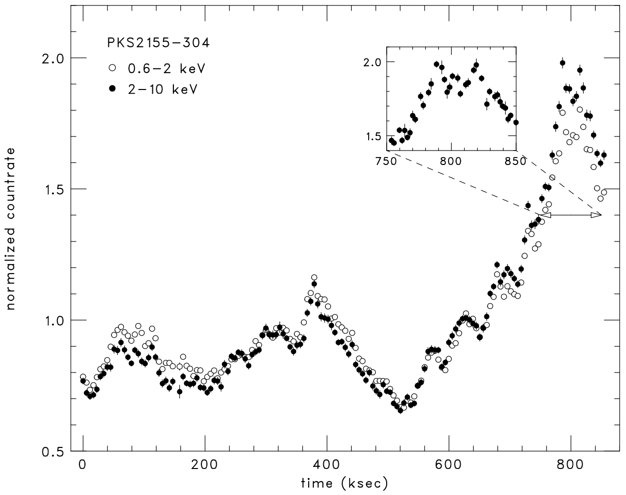
PKS2155−304
○ 0.6−2 keV
● 2−10 keV
normalized countrate
time (ksec)
0.5
1.0
1.5
2.0
0
200
400
600
800
1.5
2.0
750
800
850

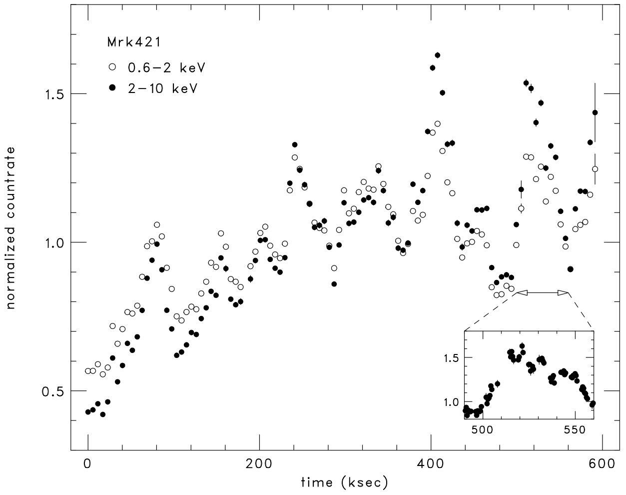
Mrk421
○ 0.6−2 keV
● 2−10 keV
normalized countrate
time (ksec)
0.5
1.0
1.5
0
200
400
600
1.0
1.5
500
550

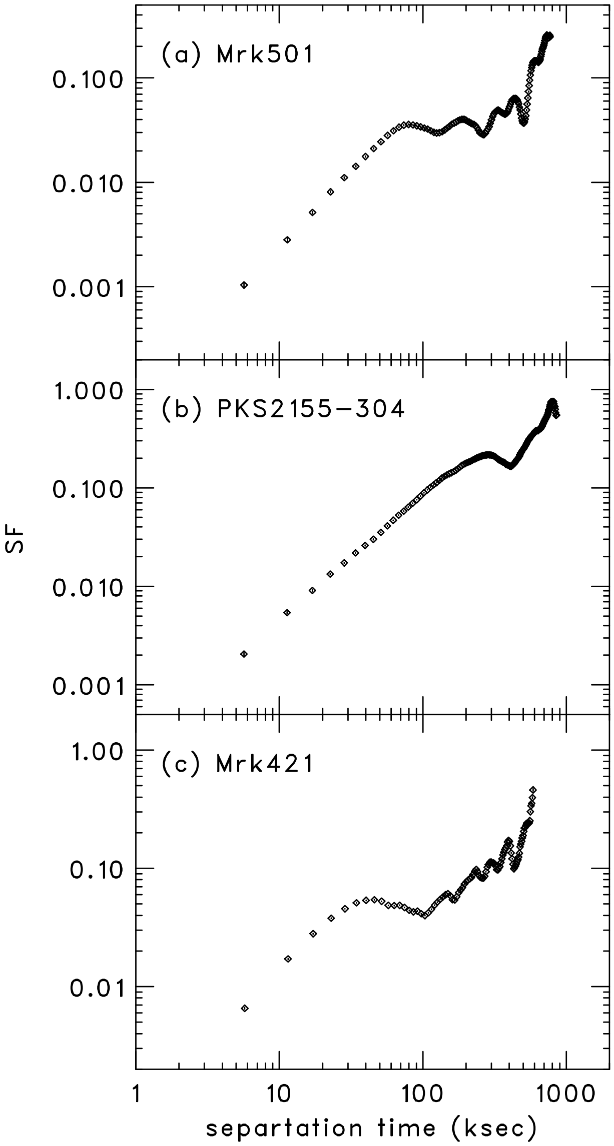
(a) Mrk501
0.100
0.010
0.001
(b) PKS2155−304
1.000
0.100
0.010
0.001
SF
(c) Mrk421
1.00
0.10
0.01
1
10
100
1000
separation time (ksec)

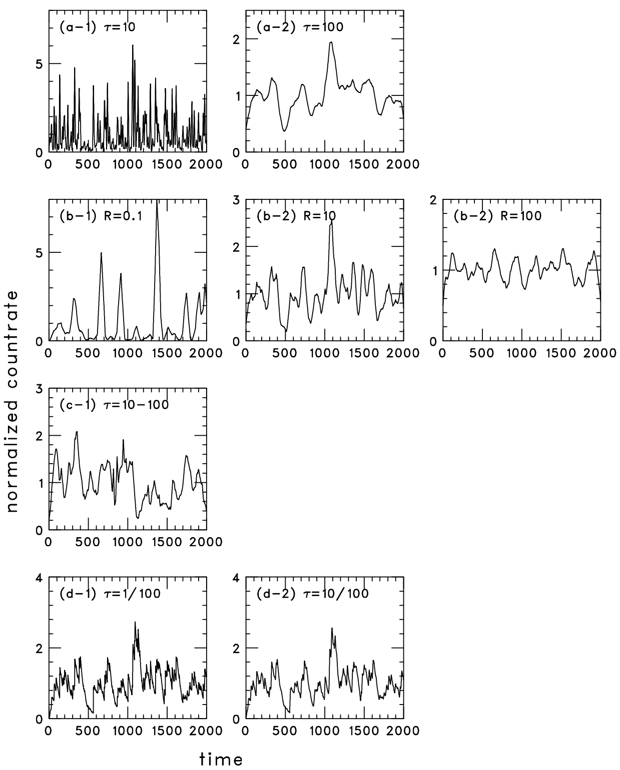
(a−1) τ=10
(a−2) τ=100
(b−1) R=0.1
(b−2) R=10
(b−2) R=100
(c−1) τ=10−100
(d−1) τ=1/100
(d−2) τ=10/100
normalized countrate
time
0
500
1000
1500
2000

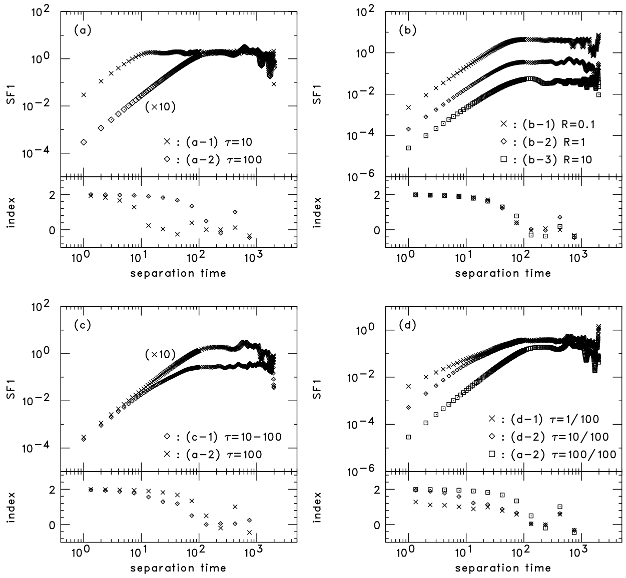
(a)
(×10)
× : (a−1) τ=10
◇ : (a−2) τ=100
(b)
× : (b−1) R=0.1
◇ : (b−2) R=1
□ : (b−3) R=10
(c)
(×10)
◇ : (c−1) τ=10−100
× : (a−2) τ=100
(d)
× : (d−1) τ=1/100
◇ : (d−2) τ=10/100
□ : (a−2) τ=100/100
SF1
index
separation time

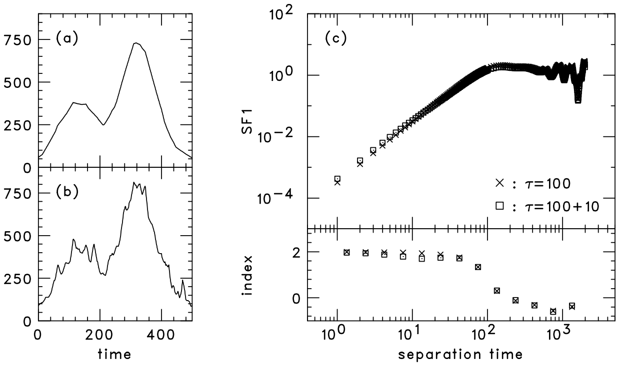
(a)
(b)
(c)
time
SF1
index
separation time
× : τ=100
□ : τ=100+10

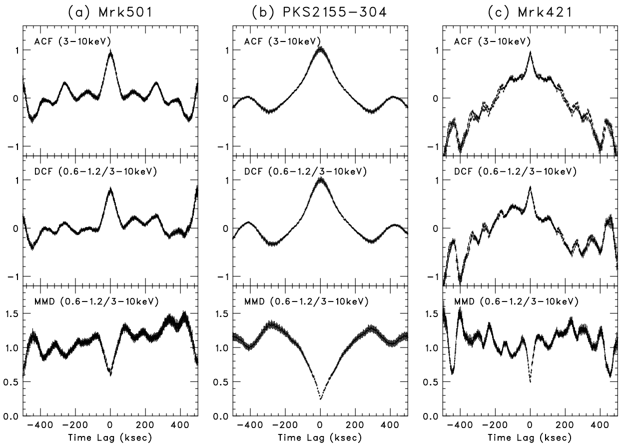
(a) Mrk501
(b) PKS2155−304
(c) Mrk421
ACF (3−10keV)
DCF (0.6−1.2/3−10keV)
MMD (0.6−1.2/3−10keV)
Time Lag (ksec)

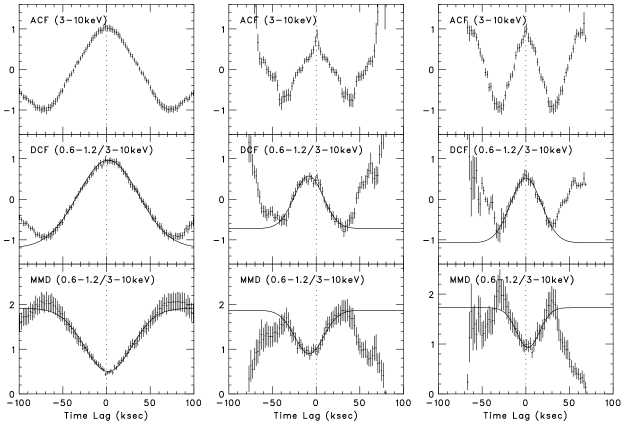
(a) Flare1
(b) Flare2
(c) Flare3
ACF (3−10keV)
DCF (0.6−1.2/3−10keV)
MMD (0.6−1.2/3−10keV)
Time Lag (ksec)

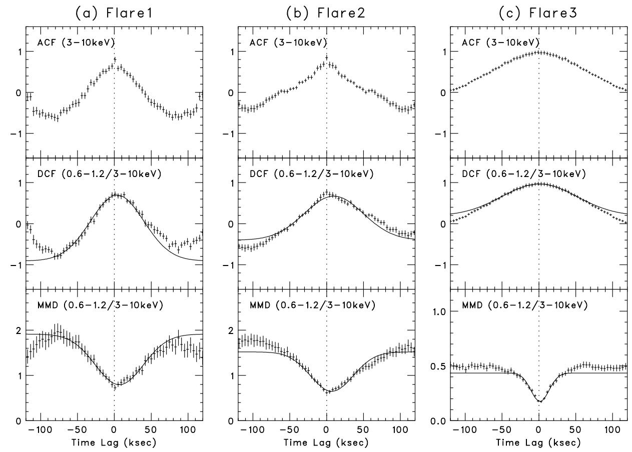
(a) Flare1
(b) Flare2
(c) Flare3
ACF (3−10keV)
DCF (0.6−1.2/3−10keV)
MMD (0.6−1.2/3−10keV)
1
0
−1
2
1
0
1.0
0.5
0.0
−100
−50
0
50
100
Time Lag (ksec)

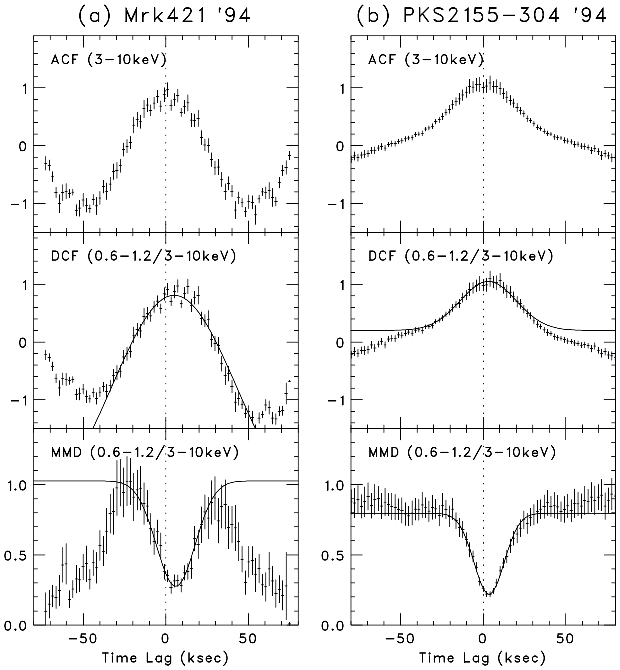
(a) Mrk421 '94
(b) PKS2155−304 '94
ACF (3−10keV)
DCF (0.6−1.2/3−10keV)
MMD (0.6−1.2/3−10keV)
1
0
−1
1.0
0.5
0.0
−50
0
50
Time Lag (ksec)

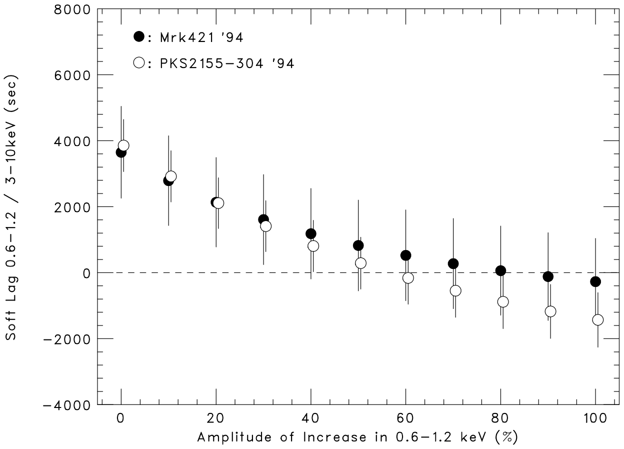
●: Mrk421 '94
○: PKS2155−304 '94
Soft Lag 0.6−1.2 / 3−10keV (sec)
8000
6000
4000
2000
0
−2000
−4000
0
20
40
60
80
100
Amplitude of Increase in 0.6−1.2 keV (%)